SAND2022-5678C

ARMA 22-640

A New Constitutive Model for Rock Salt Viscoplasticity: Formulation, Implementation, and Demonstrations

Benjamin Reedlunn[1]

[1] *Sandia National Laboratories, Albuquerque, New Mexico, USA*

ABSTRACT: This paper presents the formulation, implementation, and demonstration of a new, largely phenomenological, model for the damage-free (micro-crack-free) thermomechanical behavior of rock salt. Unlike most salt constitutive models, the new model includes both drag stress (isotropic) and back stress (kinematic) hardening. The implementation utilizes a semi-implicit scheme and a fall-back fully-implicit scheme to numerically integrate the model's differential equations. Particular attention was paid to the initial guesses for the fully-implicit scheme. Of the four guesses investigated, an initial guess that interpolated between the previous converged state and the fully saturated hardening state had the best performance. The numerical implementation was then used in simulations that highlighted the difference between drag stress hardening versus combined drag and back stress hardening. Simulations of multi-stage constant stress tests showed that only combined hardening could qualitatively represent reverse (inverse transient) creep, as well as the large transient strains experimentally observed upon switching from axisymmetric compression to axisymmetric extension. Simulations of a gas storage cavern subjected to high and low gas pressure cycles showed that combined hardening led to substantially greater volume loss over time than drag stress hardening alone.

1 INTRODUCTION

Rock salt constitutive models are used to simulate the evolution of mines, boreholes, storage caverns for gases and liquids, and nuclear waste repositories in rock salt formations. A wide variety of models have been proposed for rock salt, yet even the damage-free (micro-crack-free) thermo-viscoplastic behavior remains difficult to capture. The Munson-Dawson model, for example, was recently extended in Reedlunn et al. (2022), but it still cannot capture monotonic hardening behavior over the full range of strain rates typically utilized in laboratory tests (10^{-12} to 10^{-4} 1/s), or transient non-monotonic hardening behaviors, such as the Bauschinger effect and reverse (inverse transient) creep (Reedlunn, 2020, Section 1).

Numerical integration of most salt constitutive models is also a challenging endeavor, because the ordinary differential equations (ODEs) are usually highly non-linear and "stiff". (See Press et al. (2007, Section 17.5) for a discussion of stiff ODEs.) Explicit time integration of stiff ODEs leads to small time steps due to numerical stability limitations. Fully-implicit time integration, on the other hand, avoids such stability limitations, but it can be computationally demanding and does not always converge.

This paper presents a new rock salt constitutive model (Section 2), a method to numerically integrated it (Section 3), and demonstrations of its behavior (Section 4). Model development was influenced by a variety of models for metals (see J. Chaboche (2008) for a review) and the Yahya et al. (2000) model for salt. The model formulation was recently presented in Reedlunn (2022), but it is repeated herein for completeness. The numerical implementation strives for computational efficiency and robustness through use of carefully selected numerical techniques. The demonstrations involve cycling loading in order to draw out the difference between pure drag stress (isotropic) hardening vs. combined drag and back stress (isotropic and kinematic) hardening. Back stress hardening is not included in many salt constitutive models, but Reed-

lunn (2022) showed the addition of a back stress allowed the model to capture salt behavior over strain rates ranging from 10^{-12} to 10^{-4} 1/s at temperatures from 293 to 333 K, as well as the Bauschinger effect.

2 MODEL FORMULATION

Several preliminaries bear mentioning before defining the model formulation. First, compressive strains and stresses are treated as positive. Second, variables represented by capital letters are material constants, while variables represented by lower case letters are functions of other variables. Third, this section presents the model in an infinitesimal strain setting for simplicity, but the model can be easily extended into the finite deformation realm using hypoelasticity.

The model additively decomposes the total strain rate $\dot{\boldsymbol{\varepsilon}}$ into an elastic strain rate $\dot{\boldsymbol{\varepsilon}}^{\mathrm{el}}$, a thermal strain rate $\dot{\boldsymbol{\varepsilon}}^{\mathrm{th}}$, and a viscoplastic strain rate $\dot{\boldsymbol{\varepsilon}}^{\mathrm{vp}}$:

$$\dot{\boldsymbol{\varepsilon}} = \dot{\boldsymbol{\varepsilon}}^{\mathrm{el}} + \dot{\boldsymbol{\varepsilon}}^{\mathrm{th}} + \dot{\boldsymbol{\varepsilon}}^{\mathrm{vp}}. \tag{1}$$

The elastic behavior utilizes generalized Hooke's law in rate form to relate $\dot{\boldsymbol{\varepsilon}}^{\mathrm{el}}$, the fourth-order isotropic elastic stiffness tensor $\mathbb{E}$, and the stress rate $\dot{\boldsymbol{\sigma}}$:

$$\dot{\boldsymbol{\sigma}} = \mathbb{E} : \dot{\boldsymbol{\varepsilon}}^{\mathrm{el}} = \mathbb{E} : \left(\dot{\boldsymbol{\varepsilon}} - \dot{\boldsymbol{\varepsilon}}^{\mathrm{th}} - \dot{\boldsymbol{\varepsilon}}^{\mathrm{vp}}\right) \tag{2}$$

$$\mathbb{E} = \left(E_1 - \tfrac{2}{3}\, E_2\right) \boldsymbol{I} \otimes \boldsymbol{I} + 2\, E_2\, \mathbb{I}, \tag{3}$$

where E_1 is the bulk modulus, E_2 is the shear modulus, $\boldsymbol{I}$ is the second-order identity tensor, and $\mathbb{I}$ is the fourth-order symmetric identity tensor. The thermal strain portion of the model is simply

$$\dot{\boldsymbol{\varepsilon}}^{\mathrm{th}} = -A\, \dot{\theta}\, \boldsymbol{I}, \tag{4}$$

where A is the coefficient of thermal expansion, and θ is the absolute temperature. The viscoplastic strain rate is additively decomposed into a pressure solution strain rate $\dot{\boldsymbol{\varepsilon}}^{\,\mathrm{ps}}$ and a dislocation glide strain rate $\dot{\boldsymbol{\varepsilon}}^{\,\mathrm{dg}}$:

$$\dot{\boldsymbol{\varepsilon}}^{\mathrm{vp}} = \dot{\boldsymbol{\varepsilon}}^{\,\mathrm{ps}} + \dot{\boldsymbol{\varepsilon}}^{\,\mathrm{dg}}. \tag{5}$$

The $\dot{\boldsymbol{\varepsilon}}^{\,\mathrm{ps}}$ branch captures steady-state viscoplastic behavior at low stresses. This branch utilizes the following flow rule:

$$\dot{\boldsymbol{\varepsilon}}^{\,\mathrm{ps}} = \dot{\tilde{\varepsilon}}^{\,\mathrm{ps}} \frac{\partial \tilde{\sigma}^{\,\mathrm{ps}}}{\partial \boldsymbol{\sigma}}, \tag{6}$$

where $\dot{\tilde{\varepsilon}}^{\,\mathrm{ps}}$ and $\tilde{\sigma}^{\,\mathrm{ps}}$ are the equivalent pressure solution strain rate and stress, respectively. Pressure solution viscoplasticity is taken to be independent of the mean stress $\sigma^{\mathrm{m}} = \mathrm{tr}(\boldsymbol{\sigma})/3$ and driven entirely by the deviatoric stress $\boldsymbol{\sigma}^{\mathrm{dev}}$, so the pressure solution stress is simply

$$\boldsymbol{\sigma}^{\,\mathrm{ps}} = \boldsymbol{\sigma}^{\mathrm{dev}} = \boldsymbol{\sigma} - \sigma^{\mathrm{m}}\, \boldsymbol{I}. \tag{7}$$

This deviatoric stress tensor is reduced to a scalar equivalent (von Mises) pressure solution stress as

$$\tilde{\sigma}^{\,\mathrm{ps}} = \sqrt{\tfrac{3}{2}\, \boldsymbol{\sigma}^{\,\mathrm{ps}} : \boldsymbol{\sigma}^{\,\mathrm{ps}}}. \tag{8}$$

The equivalent pressure solution strain rate is given by

$$\dot{\tilde{\varepsilon}}^{\,\mathrm{ps}} = P_1\, \exp\left(-\frac{P_2}{\theta}\right) \frac{\tilde{\sigma}^{\,\mathrm{ps}}}{\theta}, \tag{9}$$

where P_j are material constants (Spiers et al., 1990). Eq. (9) assumes any non-zero $\tilde{\sigma}^{\,\mathrm{ps}}$ causes pressure solution flow, such that the pressure solution quasi-static (rate-independent) yield surface is simply a point at $\boldsymbol{\sigma} = 0$.

The dislocation glide branch $\dot{\boldsymbol{\varepsilon}}^{\,\mathrm{dg}}$ dominates transient viscoplastic behavior at low stresses, and all viscoplastic behavior at medium to high stresses. Dislocation glide utilizes the following flow rule,

$$\dot{\boldsymbol{\varepsilon}}^{\,\mathrm{dg}} = \dot{\tilde{\varepsilon}}^{\,\mathrm{dg}} \frac{\partial \tilde{\sigma}^{\,\mathrm{dg}}}{\partial \boldsymbol{\sigma}}, \tag{10}$$

where $\dot{\tilde{\varepsilon}}^{\,\mathrm{dg}}$ and $\tilde{\sigma}^{\,\mathrm{dg}}$ are the equivalent dislocation glide strain rate and stress, respectively. In contrast to the pressure solution branch and the majority of other salt models, the model assumes dislocation glide is driven by a dislocation glide stress

$$\boldsymbol{\sigma}^{\,\mathrm{dg}} = \boldsymbol{\sigma}^{\mathrm{dev}} - \boldsymbol{b} \tag{11}$$

that includes $\boldsymbol{b}$, a second-order tensor called the back stress. In the metals literature, the dislocation glide stress and back stress are also known as the effective stress and internal stress, respectively*. With the definition in Eq. (11), the equivalent (von Mises) dislocation glide stress is

$$\tilde{\sigma}^{\,\mathrm{dg}} = \sqrt{\tfrac{3}{2}\, \boldsymbol{\sigma}^{\,\mathrm{dg}} : \boldsymbol{\sigma}^{\,\mathrm{dg}}}. \tag{12}$$

Unlike the pressure solution branch, the dislocation glide branch has a finite size, quasi-static, yield surface, defined as

$$g = \tilde{\sigma}^{\,\mathrm{dg}} - G_0\, y, \tag{13}$$

where G_0 is a material constant and y is an isotropic hardening variable called the drag stress that evolves from a positive initial value Y_0 to some positive value. By default, $G_0 = E_2 \times 10^{-10}/Y_0$, which makes

*This effective stress should not be confused with the Terzaghi effective stress utilized in the poromechanics literature.

the $g = 0$ surface typically very small relative to $\tilde{\sigma}^{\,\mathrm{dg}}$. The equivalent dislocation glide strain rate is

$$\dot{\tilde{\varepsilon}}^{\,\mathrm{dg}} = \begin{cases} 0 & \text{for } g < 0 \\ G_1 \exp\left(-\dfrac{G_2}{\theta}\right) \left[\sinh\left(\dfrac{\tilde{\sigma}^{\,\mathrm{dg}}}{y}\right)\right]^{G_3} & \text{for } g \geq 0 \end{cases}, \tag{14}$$

where G_j are material constants. The $g \geq 0$ expression applies for both transient and steady-state creep, but it is motivated by the classic steady-state creep expression by Garofalo (1963).

The drag stress y evolves according to the following differential equation:

$$\dot{y} = Y_1 \left(\frac{Y_1}{y}\right)^{Y_2} \left(1 - \frac{y}{\bar{y}}\right) \dot{\tilde{\varepsilon}}^{\,\mathrm{dg}}, \tag{15}$$

where

$$\bar{y} = \frac{\bar{\sigma} - \bar{b}}{\sinh^{-1}\left\{\left[\dfrac{\dot{\tilde{\varepsilon}}^{\,\mathrm{dg}}}{G_1 \exp\left(-G_2/\theta\right)}\right]^{1/G_3}\right\}} \tag{16}$$

is the drag stress saturation ($\bar{y} \geq Y_0$),

$$\bar{\sigma} = Y_4 \sinh^{-1}\left\{\left[\frac{\dot{\tilde{\varepsilon}}^{\,\mathrm{dg}}}{Y_3 \exp\left(-G_2/\theta\right)}\right]^{1/Y_5}\right\} \tag{17}$$

is the equivalent (von Mises) stress saturation, $\bar{b}$ is the equivalent back stress saturation (discussed below), and Y_j are material parameters.

The back stress has a similar, yet different, set of evolution equations. Following J.-L. Chaboche (1986), $\boldsymbol{b}$ is decomposed as

$$\boldsymbol{b} = \sum_{j=1}^{2} \boldsymbol{b}_j, \tag{18}$$

where $\boldsymbol{b}_1$ is a short range, quickly evolving, back stress and $\boldsymbol{b}_2$ is a long range, slowly evolving, back stress. Each back stress has an equivalent back stress defined as

$$\tilde{b}_j = \sqrt{\frac{3}{2}\, \boldsymbol{b}_j : \boldsymbol{b}_j}. \tag{19}$$

Each back stress begins at $\boldsymbol{B}_{j0}$, which must be deviatoric ($\mathrm{tr}(\boldsymbol{B}_{j0}) = 0$) and is set to the zero tensor $\boldsymbol{0}$ by default. As deformation proceeds, each back stress evolves according to

$$\dot{\boldsymbol{b}}_j = B_{j1} \left(\frac{2}{3}\, \dot{\boldsymbol{\varepsilon}}^{\,\mathrm{dg}} - \frac{\boldsymbol{b}_j}{\bar{b}_j}\, \dot{\tilde{\varepsilon}}^{\,\mathrm{dg}}\right), \tag{20}$$

where

$$\bar{b}_j = B_{j2}\, B_{j3} \tanh\left(\frac{\bar{\sigma}}{B_{j3}}\right) \tag{21}$$

is the j^{th} equivalent back stress saturation and B_{jk} are material constants. Analogous to Eq. (18), the equivalent back stresses can be summed as

$$\tilde{b} = \sum_{j=1}^{2} \tilde{b}_j \qquad \text{and} \qquad \bar{b} = \sum_{j=1}^{2} \bar{b}_j. \tag{22}$$

All materials parameters should be non-negative to obtain typical material behavior. Furthermore, P_1, G_1, Y_1, Y_3, Y_4, Y_6, B_{j2}, B_{j3}, and $1 - \sum_{j=1}^{2} B_{j2}$ each must be non-negative to ensure y, $\bar{y}$, $\bar{b}_j$, $\bar{\sigma}$, $\dot{\tilde{\varepsilon}}^{\,\mathrm{ps}}$, $\dot{\tilde{\varepsilon}}^{\,\mathrm{dg}}$ are each non-negative.

2.1 Discussion

A thorough discussion of the model formulation will be published at a later date, but some aspects are important enough to list here:

1. The model assumes that $\dot{\boldsymbol{\varepsilon}}^{\,\mathrm{ps}}$ and $\dot{\boldsymbol{\varepsilon}}^{\,\mathrm{dg}}$ are largely independent processes because pressure solution occurs along the grain boundaries, while dislocation glide occurs inside the grains.

2. The pressure solution branch consists solely of steady-state deformation, without any hardening (transient strain). This means $\boldsymbol{b}$ and y in the dislocation glide branch are responsible for all hardening.

3. Some loose physical meaning can be attached to $\boldsymbol{b}$ and y. The back stress represents kinematic hardening due to heterogenously distributed dislocation substructures, such as sub-grains and wavy slip bands produced by dislocation climb and cross-slip, respectively (Carter et al., 1993). These substructures are commonly observed at low to medium strain rates ($10^{-12} \leq \dot{\tilde{\varepsilon}}^{\,\mathrm{vp}} \leq 10^{-8}$ 1/s) and low to high temperatures ($293 \leq \theta \leq 973$ K). The drag stress represents isotropic hardening due to more uniform dislocation distributions, as are observed at higher strain rates over the same temperature range (Raj and Pharr, 1989).

4. Both hardening evolution equations (Eqs. (15) and (20)) conform to the Bailey-Orowan concept, in which the hardening rate is the result of a competition between a strain hardening term and a strain (a.k.a. dynamic) recovery term. Hardening saturates when the hardening and recovery rates balance one another ($\dot{y} = 0$ and $\dot{\boldsymbol{b}}_j = \boldsymbol{0}$).

5. During proportional loading and at hardening saturation, the stresses $\boldsymbol{\sigma}^{\mathrm{dev}}$ and $\boldsymbol{b}$ are coaxial, so Eqs. (11) and (12) reduce a scalar equation:

$$\tilde{\sigma}^{\mathrm{dg}} = \tilde{\sigma} - \tilde{b}. \tag{23}$$

6. At hardening saturation, $\tilde{b}_j = \bar{b}_j$, $y = \bar{y}$, such that Eqs. (14), (16), (17) and (23) combine to give $\tilde{\sigma} = \bar{\sigma}$. Inverting the expression for $\bar{\sigma}$ in Eq. (17) results in the Garofalo (1963) steady-state dislocation glide strain rate expression:

$$\dot{\tilde{\varepsilon}}^{\mathrm{dg}} = Y_3 \exp\left(-\frac{G_2}{\theta}\right)\left[\sinh\left(\frac{\bar{\sigma}}{Y_4}\right)\right]^{Y_5}. \tag{24}$$

2.2 Calibrations

Reedlunn et al. (2022) presented four calibrations of this model against tests on Waste Isolation Pilot Plant salt at $293 \leq \theta \leq 333$ K. Two of the four calibrations are utilized herein: Calibration 1A1 and Calibration 1C. Both calibrations have the same steady-state strain rate behavior. Calibration 1A1 uses only drag stress hardening to capture constant stress tests with $10 \leq \tilde{\sigma} \leq 18$ MPa. Calibration 1C uses both drag and back stress hardening to capture constant stress tests with $4 \leq \tilde{\sigma} \leq 18$ MPa and constant strain rate tests at rates ranging from 10^{-6} to 10^{-4} 1/s. As one might expect, Calibration 1C more accurately captures the transient strains corresponding to constant stress tests with $4 \leq \tilde{\sigma} \leq 8$ MPa.

3 NUMERICAL IMPLEMENTATION

The model was implemented in Sandia's Sierra/SolidMechanics (2021) code using the C++ programming language. Sierra's hypoelastic framework uses the Green-McInnis rate of the Cauchy stress and integrates constitutive models in the unrotated configuration. This approach replaces the strain rates and stress rates in Section 2 with the unrotated rate of deformation and the unrotated rate of the Cauchy stress. In the absence of rotations, the unrotated rate of deformation coincides with the logarithmic strain rate and the unrotated Cauchy stress rate coincides with the Cauchy stress rate.

As mentioned in Section 1, viscoplastic models are notoriously difficult to numerically integrate because the ODEs are stiff. The implementation of the model pursued herein first attempts to integrate the ODEs with a Richardson extrapolation of the semi-implicit backward Euler method[†], and, if that approach fails, then employs the fully-implicit backward Euler method.

The Richardson extrapolated semi-implicit backward Euler method is clearly demonstrated in Hofstetter (2014, Chapter 1), but a short summary follows. The method approximates the time derivatives with backward Euler expressions, thus creating a system of non-linear algebraic equations. These algebraic equations are first approximately solved in one large step over the full time interval, producing a solution $\boldsymbol{x}_1$. The algebraic equations are then approximately solved again over the same time interval, except it is broken into two half sub-steps, thereby producing a more accurate solution $\boldsymbol{x}_2$. In both cases, the solutions $\boldsymbol{x}_1$ and $\boldsymbol{x}_2$ are arrived at using only one Newton iteration per time step, or per half time step, to reduce computational cost. The Richardson extrapolation of the two solutions to a second order-accurate solution, with respect to time, turns out to be simply $\boldsymbol{x} = 2\,\boldsymbol{x}_2 - \boldsymbol{x}_1$. Furthermore, having two solutions allows one to obtain an error estimate $\boldsymbol{e} = \boldsymbol{x}_2 - \boldsymbol{x}_1$. If the error is acceptable, then a norm of $\boldsymbol{e}$ is compared against accuracy targets to suggest the next time step size to the host code (either a material point driver or a momentum balance code). This adaptive time stepping makes the host code take small time steps when the solution is changing rapidly and large steps when the solution is changing gradually. If the error $\boldsymbol{e}$ is unacceptable, then the model implementation falls back to the fully-implicit backward Euler method.

In the fully-implicit backward Euler method, the same system of non-linear algebraic equations are solved over the full time interval using an iterative solver. The iterative solver utilized herein is Newton's method, coupled with a line search routine, similar to that described in Reedlunn (2018, Chapter 3). The iterations start from some initial guess $\boldsymbol{x}_0$ and continue until the error is sufficiently small, or the maximum number of iterations is reached. If the fully-implicit scheme converges, the model implementation accepts the solution and suggests a smaller time step to the host code for the next time step to give the semi-implicit scheme a higher chance of success on the next time step.

The number of iterations n_{itr} for the fully-implicit scheme to converge to an acceptable solution can be quite sensitive to the choice of $\boldsymbol{x}_0$. To probe this sensitivity, a series of material point simulations were performed with Calibration 1C over

[†]Note that some authors use the phrase "semi-implicit" to indicate explicit integration of certain ODEs and implicit integration other ODEs. Herein, "semi-implicit Euler method" indicates that a single implicit iteration is utilized on all ODEs, rather than iterating until a residual is nearly zero.

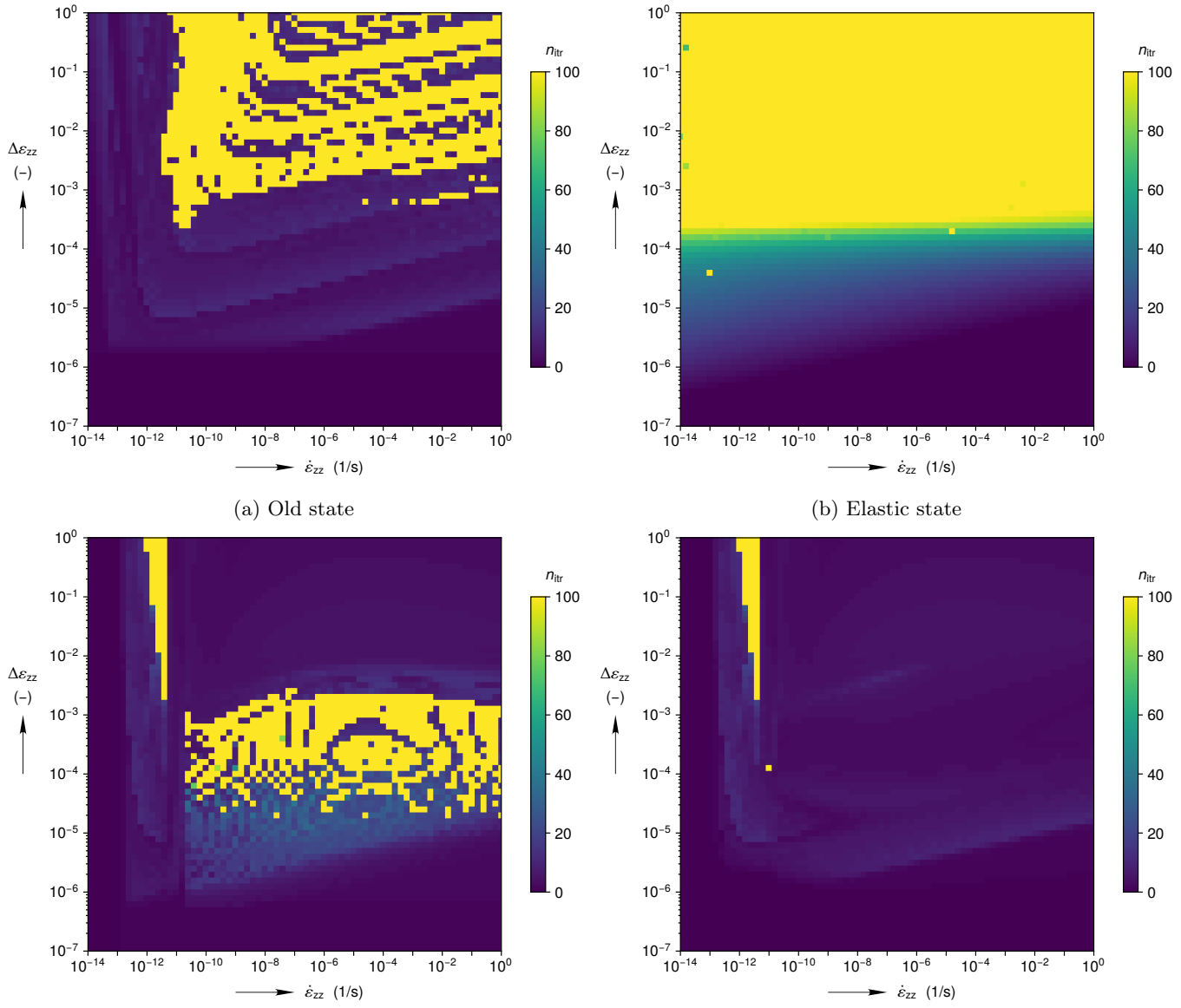

(a) Old state

(b) Elastic state

(c) Saturated hardening state

(d) Interpolated state

Figure 1: Number of iterations to converge for (almost) uniaxial stress at various strain rates and strain increments. All cases began in an unhardened state ($y = Y_0$ and $\boldsymbol{b}_i = \boldsymbol{0}$).

a range of strain rates and strain increments. All cases started from an unhardened state ($y = Y_0$ and $\boldsymbol{b}_i = \boldsymbol{0}$). (Future studies may consider convergence from pre-hardened states.) The strain rate components were prescribed as

$$[\dot{\varepsilon}_{ij}] = \begin{bmatrix} -\dot{\varepsilon}_{zz}/2 & 0 & 0 \\ 0 & -\dot{\varepsilon}_{zz}/2 & 0 \\ 0 & 0 & \dot{\varepsilon}_{zz} \end{bmatrix}, \qquad (25)$$

to produce nearly uniaxial stress at an axial strain rate of $\dot{\varepsilon}_{zz}$ over a time increment Δt, producing an axial strain increment of $\Delta\varepsilon_{zz}$. The semi-implicit scheme was skipped, and the maximum number of fully-implicit iterations permitted was $n_{itr} = 100$. The results corresponding to four different initial guesses are shown in Fig. 1.

Perhaps the most straightforward initial guess is the old, previously converged, state $\boldsymbol{x}_0 = \boldsymbol{x}_0^{old}$. The equivalent stress corresponding to the old state is denoted as $\tilde{\sigma}_0^{old}$. This simple initial guess converged in less than 30 iterations when $\dot{\varepsilon}_{zz} \leq 3 \times 10^{-12}$ 1/s and $\Delta\varepsilon_{zz} \leq 2 \times 10^{-4}$, as shown in Fig. 1a, but it frequently failed to converge at higher strain rates and increments.

Perhaps the most commonly used initial guess in plasticity implementations treats the total strain increment from the host code as a purely elastic strain increment, $\boldsymbol{x}_0 = \boldsymbol{x}_0^{el}$. This purely elastic strain increment produces an initial guess for $\tilde{\sigma}$ denoted as the trial, elastic, equivalent stress $\tilde{\sigma}_0^{el}$. Purely elastic initial guesses converged for small $\Delta\varepsilon_{zz}$, as shown in Fig. 1b, but failed for $\Delta\varepsilon_{zz} > 2 \times 10^{-4}$.

Schreyer (2002) recognized the poor performance of $\boldsymbol{x}_0^{\text{old}}$ and $\boldsymbol{x}_0^{\text{el}}$, which led him to propose another initial guess: a purely viscoplastic strain increment with fully saturated hardening and zero elastic strain increment, $\boldsymbol{x}_0 = \boldsymbol{x}_0^{\text{vp}}$. To compute $\boldsymbol{x}_0^{\text{vp}}$, one requires the trial, fully saturated, equivalent stress $\bar{\sigma}_0$ corresponding to a pure viscoplastic strain rate $\dot{\varepsilon}_{\text{zz}} = \dot{\bar{\varepsilon}}_0^{\text{vp}}$. The following equation

$$\dot{\bar{\varepsilon}}_0^{\text{vp}} = P_1 \exp\left(-\frac{P_2}{\theta}\right) \frac{\bar{\sigma}_0}{\theta} + Y_3 \exp\left(-\frac{G_2}{\theta}\right) \left[\sinh\left(\frac{\bar{\sigma}_0}{Y_4}\right)\right]^{Y_5}, \tag{26}$$

provides an implicit relationship between $\dot{\bar{\varepsilon}}_0^{\text{vp}}$ and $\bar{\sigma}_0$, but it does not have an analytical solution. One can, however, ignore interactions between the two terms in Eq. (26), solve $\dot{\bar{\varepsilon}}_0^{\text{vp}} = P_1 \exp\left(-\frac{P_2}{\theta}\right) \frac{\bar{\sigma}_0}{\theta}$ for $\bar{\sigma}_0$, solve $\dot{\bar{\varepsilon}}_0^{\text{vp}} = Y_3 \exp\left(-\frac{G_2}{\theta}\right) \left[\sinh\left(\frac{\bar{\sigma}_0}{Y_4}\right)\right]^{Y_5}$ for $\bar{\sigma}_0$, and then adopt the smaller of the two $\bar{\sigma}_0$. With $\bar{\sigma}_0$ determined, it is relatively straightforward to compute the remaining components in $\boldsymbol{x}_0^{\text{vp}}$ for materials with a von Mises flow potential (Schreyer, 2002). This initial guess generally performed better than the old and elastic states for $\Delta\varepsilon_{\text{zz}} \geq 3 \times 10^{-3}$ (see Fig. 1c), but worse for smaller strain increments.

The last initial guess considered herein combined the three previous guesses into one scheme. The following measure of expected deviatoric loading,

$$\chi = \min\left[X \left(\frac{\tilde{\sigma}_0^{\text{el}} - \tilde{\sigma}_0^{\text{old}}}{\bar{\sigma}_0 - \tilde{\sigma}_0^{\text{old}}}\right), 1\right] \tag{27}$$

where $X \geq 0$ is a tuning parameter, was used to construct the following initial guess,

$$\boldsymbol{x}_0 = \boldsymbol{x}_0^{\text{in}} = \begin{cases} \boldsymbol{x}_0^{\text{el}}, & \text{for } \chi \leq 0 \\ \boldsymbol{x}_0^{\text{old}} + \chi \left(\boldsymbol{x}_0^{\text{sat}} - \boldsymbol{x}_0^{\text{old}}\right), & \text{for } \chi > 0. \end{cases} \tag{28}$$

In words, if deviatoric unloading is expected, then $\boldsymbol{x}_0^{\text{in}}$ uses an elastic strain increment. If deviatoric loading is expected, then $\boldsymbol{x}_0^{\text{in}}$ linearly interpolates between the old state and the saturated hardening state, but not beyond the saturated hardening state. The convergence behavior corresponding to $0 \leq X \leq 1$ was studied in $\Delta X = 0.1$ increments, leading to the selection of $X = 0.2$. The performance of this initial guess scheme is shown in Fig. 1d, where almost every case converged in $n_{\text{itr}} < 30$. The sliver of non-convergence at $3.9 \times 10^{-13} \leq \dot{\varepsilon}_{\text{zz}} \leq 4 \times 10^{-12}$ 1/s and $\Delta\varepsilon_{\text{zz}} \geq 2 \times 10^{-3}$ is not ideal, but probably not very important because large strain increments at such slow strain rates are rare. This initial guess scheme was used for the simulations discussed in the following section.

4 DEMONSTRATIONS

Two demonstrations are presented, both of which compare the behavior of Calibration 1A1 (only drag stress hardening) against Calibration 1C (combined drag stress and back stress hardening).

4.1 Multi-stage constant stress simulations

The first demonstration explores the constant stress behavior after stress drops of varying size at $\theta = 300$ K. The simulations all began with hydrostatic loading to a Cauchy stress of $\sigma_{\text{rr}} = \sigma_{\theta\theta} = \sigma_{\text{zz}} = 20$ MPa, which induced a logarithmic axial strain of $\varepsilon_{\text{zz}}(t_0^-)$, where t_0^- was the instant in time before $t_0 = 0$ days. This mean stress $\sigma_{\text{m}} = \text{tr}(\boldsymbol{\sigma})/3 = 20$ MPa was held fixed over the remainder of each simulation, while the stress difference $\breve{\sigma} = \sigma_{\text{zz}} - \sigma_{\text{rr}}$ was varied by setting $\sigma_{\text{rr}} = \sigma_{\text{m}} - \breve{\sigma}/3$ and $\sigma_{\text{zz}} = 2\,\breve{\sigma}/3 + \sigma_{\text{m}}$. At t_0, $\breve{\sigma}$ was raised to 12 MPa and held for 50 days. As shown in Fig. 2a, this stress increase caused a rapid increase in ε_{zz} during the first day, but $\dot{\varepsilon}_{\text{zz}}$ gradually reduced, trending towards its steady-state rate. Note that the Calibration 1A1 strain histories were artificially shifted downward by 0.068 % strain in Fig. 2 in order to aid visual comparisons. (Both Calibration 1A1 and 1C were each fit against strain histories from constant stress tests with $\breve{\sigma} = 12$ MPa, but they still do not produce the exact same strain histories at a given stress.) The bottom plot in Fig. 2a depicts the back stress difference $\breve{b} = b_{\text{zz}} - b_{\text{rr}}$, where $\breve{b}(t_1^-) = 0.0$ and 10.0 MPa in the Calibration 1A1 and Calibration 1C simulations, respectively.

At $t_1 = 50$ days, $\breve{\sigma}$ was dropped by differing amounts in each simulation, leading to differing strain histories over the next 50 d. The Calibration 1A1 strain histories exhibit little to no transient strain, while the Calibration 1C strain histories exhibit small to large amounts of transient strain depending on the magnitude of the stress drop.

The small stress drops to $\breve{\sigma}(t_1) > 0$ keep the salt in axisymmetric compression, which leads to small amounts of forward creep ($\text{sign}(\dot{\varepsilon}_{\text{zz}}) = \text{sign}(\breve{\sigma})$) with Calibration 1A1, and reverse creep ($\text{sign}(\dot{\varepsilon}_{\text{zz}}) \neq \text{sign}(\breve{\sigma})$) with Calibration 1C. The drop to $\breve{\sigma}(t_1) = 9$ MPa produces virtually identical Calibration 1A1 and 1C strain histories in Fig. 2b, with very little transient strain from Calibration 1C because $\breve{\sigma}^{\text{dg}} = \breve{\sigma} - \breve{b}$ is small. Drops to $\breve{\sigma}(t_1) = 6$ and 3 MPa cause $\dot{\varepsilon}_{\text{zz}} > 0$ in the Calibration 1A1 simulations, yet cause $\dot{\varepsilon}_{\text{zz}} < 0$ in the Calibration 1C simulations. In both cases, $\text{sign}(\dot{\varepsilon}_{\text{zz}})$ can be explained by recognizing that Eq. (10) reduces to

$$\dot{\varepsilon}_{\text{zz}}^{\text{dg}} = \dot{\bar{\varepsilon}}^{\text{dg}} \, \text{sign}(\breve{\sigma} - \breve{b}) \tag{29}$$

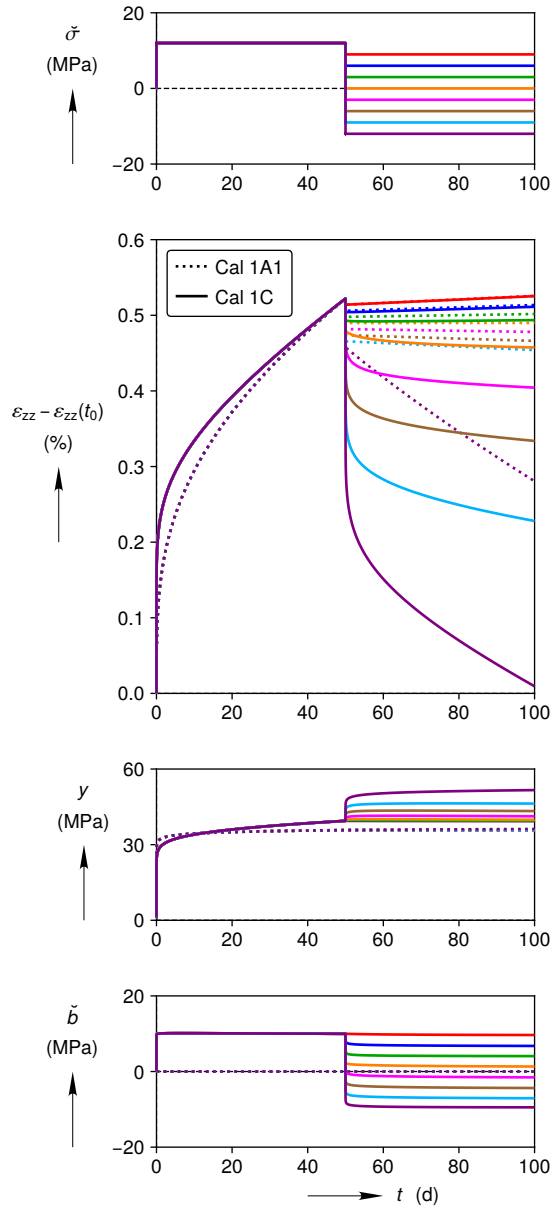

(a) Full histories

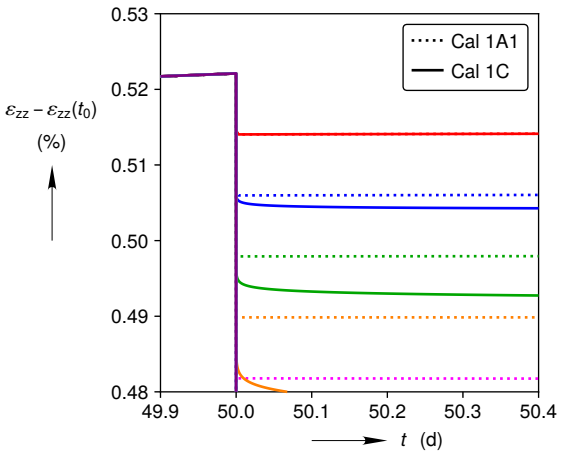

(b) Close-up view of strain histories corresponding to small stress drops

Figure 2: Multi-stage constant stress simulations with two different salt model calibrations. (Note that the Calibration 1A1 strain histories were shifted down by 0.068 % strain to more closely match the Calibration 1C strain histories.)

under axisymmetric loading. For Calibration 1A1, $\text{sign}\,(\breve{\sigma} - \breve{b}) = \text{sign}\,(\breve{\sigma})$, so $\dot{\varepsilon}_{zz}^{dg} > 0$. For Calibration 1C, $\breve{\sigma} - \breve{b} < 0$ when $\breve{\sigma}(t_1) = 6$ and 3 MPa, so $\dot{\varepsilon}_{zz}^{dg} < 0$. The Calibration 1C predictions for $\breve{\sigma}(t_1) > 0$ are qualitatively consistent with the experimental results on Asse salt in Hunsche (1988, Fig. 3), while the Calibration 1A1 predictions are not.

The large stress drops to $\breve{\sigma}(t_1) \leq 0$ place the material under hydrostatic compression or axisymmetric extension, causing both calibrations to predict $\dot{\varepsilon}_{zz} \leq 0$. Calibration 1A1 predicts very little transient strain because the material is over-hardened. Calibration 1C, on the other hand, predicts substantial amounts of transient strain because the back stress can re-harden upon a large change in $\breve{\sigma}$. The stress drop to $\breve{\sigma}(t_1) = -12$ MPa exhibits as large a transient strain magnitude as during $0 < t < t_1$, and $|\dot{\varepsilon}_{zz}(t_2)| \approx |\dot{\varepsilon}_{zz}(t_1^-)|$, where $t_2 = 100$ d, which is consistent with experimental results on Cayuta salt in Mellegard et al. (2007).

4.2 Cyclic loading of a gas storage cavern

The second demonstration is a common application of salt constitutive models: prediction of a gas storage cavern's volume loss over time. A schematic of the axisymmetric cavern geometry and boundary conditions is shown in Fig. 3. The left side of the domain was the axis of symmetry, the top was traction free, while the bottom and right sides had roller boundary conditions. The single cigar-shaped cavern had a radius and length of $L_r = 35$ m and $L_z = 600$ m, respectively. The cavern center was $L_c = 1100$ m beneath the surface. The bottom and right sides of the domain were $L_d = 4400$ m away from the cavern center. The domain was pure salt for simplicity, with a density of $\rho = 2300$ kg/m^3. Gravity was taken as 9.79 m/s^2, and the temperature was 300 K throughout the domain.

To initialize the simulations, all material points were assigned a lithostatic stress state, and a liquid pressure, equal to the lithostatic pressure, was applied to the cavern walls. (Salt cannot sustain a deviatoric stress over the long term, so it is reasonable to assume a simple lithostatic stress state at the onset.) The cavern excavation and filling with gas was simulated by linearly ramping the liquid pressure to zero while simultaneously linearly increasing the wellhead gas pressure from $p_{wh} = 0$ to 12.84 MPa. The excavation and filling was performed over 0.01 s, amounting to a virtually instantaneous process. The gas pressure within the cavern was treated as spatially uniform and equal to p_{wh}.

The value of p_{wh} was varied over the remainder of each simulation to capture the effect of storing and extracting gas from the cavern. Four cycles were applied while measuring the cavern volume v. The first cycle held $p_{\text{wh}} = 12.84$ MPa for five years, then decreased it to $p_{\text{wh}} = 6.42$ MPa virtually instantaneously (over 0.01 s), and held $p_{\text{wh}} = 6.42$ MPa for three days. The next three cycles each held $p_{\text{wh}} = 12.84$ MPa for three days and then held $p_{\text{wh}} = 6.42$ MPa for another three days. Pressurization cycles such as these are most representative of compressed air energy storage facilities, but some natural gas storage operations utilize similar cycles (Sobolik, 2022). Note that, in reality, virtually instantaneous gas pressure changes would cause adiabatic temperature changes, but this effect is ignored for simplicity.

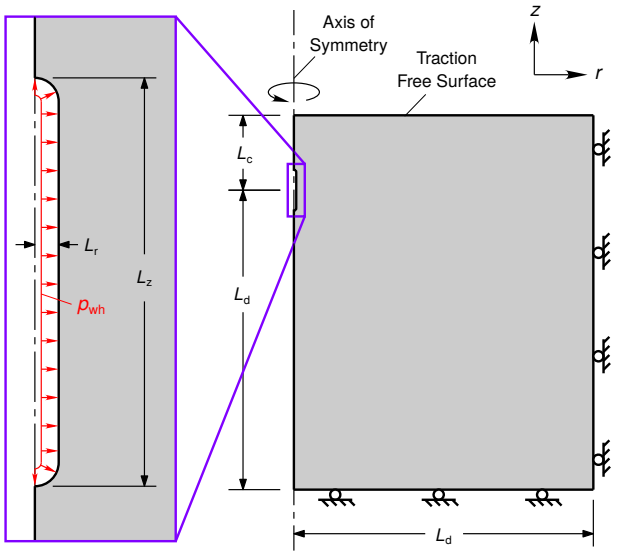

Figure 3: Axisymmetric cavern geometry and boundary conditions.

A few numerical details bear mentioning. All simulations were performed using Sierra/SolidMechanics (2021)'s implicit quasi-static finite element capability. The selective deviatoric element, which fully integrates the deviatoric response with $N_{\text{ip}} = 8$ integration points and under integrates the pressure response (similar to a q1p0 element), was used throughout the domain. Element sizes started at $L_z/100$ near the cavern and gradually grew with distance from the cavern, reaching roughly $L_z/2$ along the right and bottom boundaries. The total number of elements was $N_{\text{el}} = 13585$. The equilibrium equations were solved to a maximum relative residual norm of $R_{\max} = 10^{-7}$, where $R_{\max}$ is the L2 norm of the total residual divided by the L2 norm of the reaction loads at the roller boundary conditions. The total number of iterations throughout each simulation was roughly $N_{\text{itr}} = 12 \times 10^3$.

The salt constitutive model was evaluated about $N_{\text{el}}\, N_{\text{ip}}\, N_{\text{itr}} = 1.3 \times 10^9$ times during each simulation, and only failed to converge two times during the Calibration 1A1 simulation and six times during the Calibration 1C simulation. This suggests the numerical implementation in Section 3 is quite robust. Some of the robustness is attributed to using the interpolated state as the initial guess to the fully-implicit scheme, because the constitutive model repeatedly failed to converge in abondoned preliminary simulations that used the old state, elastic state, and saturated hardening state as the initial guess. Future studies will evaluate the constitutive model implementation in simulations involving contact constraints and/or materials other than salt.

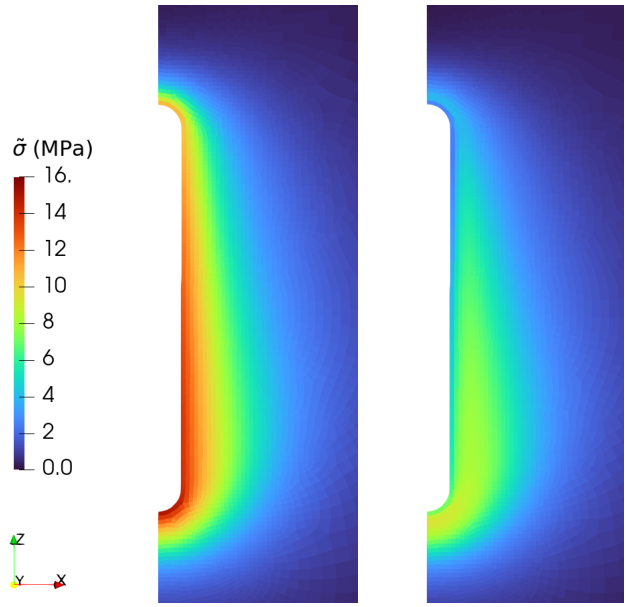

(a) $p_{\text{wh}} = 6.42$ MPa (b) $p_{\text{wh}} = 12.84$ MPa

Figure 4: Equivalent stress near the cavern at low and high wellhead pressure.

After instantaneous excavation and any p_{wh} jumps, the time step increment was allowed to grow or shrink according to the error estimate from the semi-implicit scheme described in Section 3, subject to lower and upper bounds of 0.5× and 1.1× change per time step. A systematic investigation of the time step size was not performed, but the time step size began at 10^{-3} s, grew in every case manually inspected, and eventually reached about 10 d during the first 5 yr period with $p_{\text{wh}} = 12.84$ MPa. The persistent time step growth, combined with the robustness observations mentioned above, means the fully-implicit scheme was intermittently activated during global equilibrium iterations for a given time step,

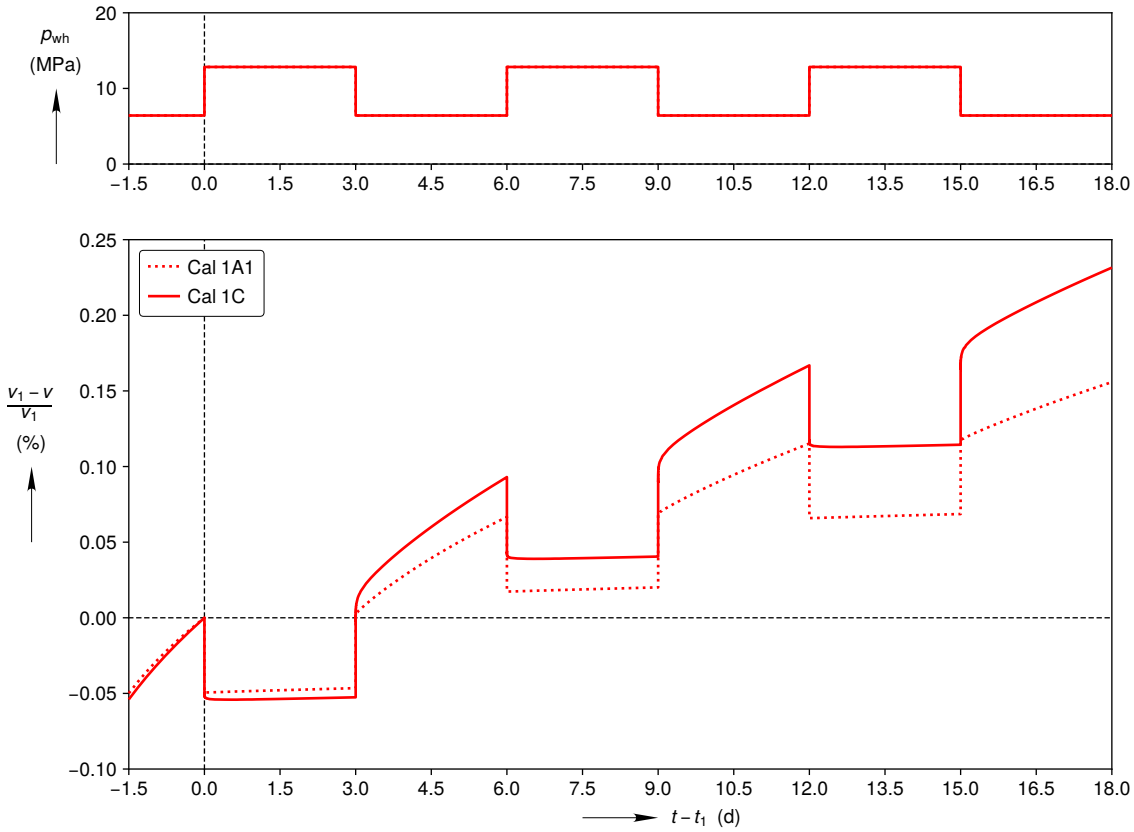

Figure 5: Cavern volume loss, relative to the end of cycle one, during cycles two through four, for two different salt model calibrations.

yet the semi-implicit scheme sufficiently reduced the error at every integration point for the last, converged, global equilibrium iteration.

The equivalent stress fields near the cavern, averaged over each element, are shown in Fig. 4 for the two wellhead pressures applied. These fields correspond to the end and halfway through cycle 4 in the Calibration 1C simulation, but they do not vary dramatically between Calibration 1A1 and 1C, or from cycle to cycle. As one might expect, low p_{wh} leads to high $\tilde{\sigma}$ near the cavern, while high p_{wh} leads to low $\tilde{\sigma}$ near the cavern. From low to high p_{wh}, the value of $\tilde{\sigma}$ drops from 14.9 MPa to 7.3 MPa, from 11.5 to 9.2 MPa, and from 6.0 to 5.5 MPa at locations 3 m, 21 m, and 57 m from the cavern's bottom surface, respectively.

The predicted cavern volume loss histories in Fig. 5 show the clear difference between Calibration 1A1, without kinematic hardening, and Calibration 1C, with kinematic hardening. To make the differences more visible, all but the very end of the first wellhead pressure cycle is omitted from Fig. 5, $t - t_1$ is the time relative to the end of cycle one, and $(v_1 - v)/v_1$ is the volume loss relative to the volume at end of cycle one v_1. When the wellhead pressure is raised to $p_{\text{wh}} = 12.84$ at $t - t_1 = 0$, both calibrations predict an elastic increase in volume of 0.05 %, but Calibration 1C predicts an additional 0.006 % volume increase due to reverse creep. This minor difference appears consistent with the difference in the $\tilde{\sigma}$ fields between Fig. 4a and Fig. 4b near the cavern, and the reverse creep responses due to small stress drops in Fig. 2b. When the wellhead pressure is decreased to $p_{\text{wh}} = 6.42$ at $t - t_1 = 3$ d, the Calibration 1A1 volume loss rate returns nearly to the same rate observed at the end of cycle one. The Calibration 1C volume loss rate, by contrast, is substantially higher than that at the end of cycle one. This difference can be explained by the y and $\breve{b}$ histories Fig. 2a: after a $\tilde{\sigma}$ drop (after a p_{wh} increase), hardening negligibly evolves in Calibration 1A1, yet the back stress substantially decreases in Calibration 1C, even after a small $\tilde{\sigma}$ drop. Once $\tilde{\sigma}$ is increased again (p_{wh} is decreased again), the Calibration 1A1 salt picks up right where it left off, while the back stress in Calibration 1C salt must substantially increase (re-harden), leading to a greater volume loss rate at $t^+ - t_1 = 3$ d than at $t^- - t_1 = 0$. At the end of cycle two ($t^- - t_1 = 6$ d), Calibration 1C predicts 39 % greater volume loss, relative to the end of cycle one, than Calibration 1A1. Cycles three and four continue the same trend, leading

one to expect dramatic differences if cycling were to continue for several years.

5 CONCLUSIONS

The transient hardening behavior of damage-free rock salt remains challenging to capture with constitutive models, and methods to numerical integrate such models are far from trivial. Accordingly, this paper reviewed a new salt constitutive model formulation, implemented it in a finite element code, and demonstrated the behaviors it predicts in two examples. One important difference between this model and others in the literature, is the addition of back stress (kinematic) hardening as well as drag stress (isotropic) hardening.

The numerical implementation first attempts to integrate the model's differential equations using a Richardson extrapolated semi-implicit scheme. This scheme produces an error estimate that can be used to suggest the next time step size to the host momentum balance code. If the semi-implicit scheme fails, the implementation falls back to a fully-implicit scheme. Four different initial guesses for the fully-implicit scheme were investigated: the previous converged state, a fully elastic state, a fully viscoplastic state, and an initial guess that interpolated between the previous converged state and the fully viscoplastic state. Comparing the number of iterations to converge over a wide range of strain increments and strain rates revealed that the interpolated initial guess performed best.

The demonstration examples brought out differences between simple drag stress hardening and combined drag and back stress hardening. Only combined hardening was able to qualitatively represent reverse creep and the large transient strains experimentally observed during multi-stage constant stress tests with stress drops (Hunsche, 1988; Mellegard et al., 2007). Simulations of a gas cavern subjected to high and low pressure cycles showed that the numerical implementation is robust enough for structural problems, and demonstrated that combined hardening predicts considerably more volume loss over time than drag stress hardening alone.

ACKNOWLEDGEMENTS

The author gratefully acknowledges the assistance of his Sandia colleagues (especially James Bean and Steve Sobolik), his Joint Project WEIMOS colleagues, and Prof. Howard Schreyer. Sandia National Laboratories is a multi-mission laboratory managed and operated by National Technology and Engineering Solutions of Sandia, LLC., a wholly owned subsidiary of Honeywell International, Inc., for the U.S. Department of Energy's National Nuclear Security Administration under contract DE-NA0003525. This research is funded by WIPP programs administered by the Office of Environmental Management (EM) of the U.S. Department of Energy. This paper describes objective technical results and analysis. Any subjective views or opinions that might be expressed in the paper do not necessarily represent the views of the U.S. Department of Energy or the United States Government. SAND2022-XXXXXC

REFERENCES

Carter, N., Horseman, S., Russell, J., and Handin, J. 1993. "Rheology of rocksalt". In: *Journal of structural geology* 15.9-10, pp. 1257–1271.

Chaboche, J.-L. 1986. "Time-independent constitutive theories for cyclic plasticity". In: *International journal of plasticity* 2.2, pp. 149–188.

Chaboche, J. 2008. "A review of some plasticity and viscoplasticity constitutive theories". In: *International journal of plasticity* 24.10, pp. 1642–1693.

Garofalo, F. 1963. "An empirical relation defining the stress dependence of minimum creep rate in metals". In: *Trans. aime* 227, pp. 351–356.

Hofstetter, G. 2014. *Computational engineering*. Springer.

Hunsche, U. 1988. "Measurement of creep in rock salt at small strain rates". In: *The mechanical behavior of salt proceedings of the second conference*. Clausthal: Trans. Tech. Publications, pp. 187–196.

Mellegard, K. D., DeVries, K. L., and Callahan, G. D. May 2007. "Lode angle effects on the creep of salt". In: *Proc. 6th conference on the mechanical behavior of salt*. Ed. by M. Wallner, K.-H. Lux, W. Minkley, and H. R. H. Jr. Taylor & Francis.

Press, W. H., Teukolsky, S. A., Vetterling, W. T., and Flannery, B. P. 2007. *Numerical recipes*. Third. Cambridge university press Cambridge.

Raj, S. V. and Pharr, G. 1989. "Creep substructure formation in sodium chloride single crystals in the power law and exponential creep regimes". In: *Materials science and engineering: a* 122.2, pp. 233–242.

Reedlunn, B. Nov. 2018. *Enhancements to the Munson-Dawson model for rock salt*. Tech. rep. SAND2018-12601. Albuquerque, NM, USA: Sandia National Laboratories.

Reedlunn, B. Oct. 2020. *Status of a new thermomechanical constitutive model for rock salt*. Memorandum. SAND2020-11023 CTF.

Reedlunn, B. 2022. "A new rock salt constitutive model with back stress and drag stress hardening". In: *The mechanical behavior of salt X*. (accepted).

Reedlunn, B., Argüello, J. G., and Hansen, F. D. 2022. "A reinvestigation into munson's model for room closure in bedded rock salt". In: *International journal of rock mechanics and mining sciences* 151.

Schreyer, H. 2002. "On time integration of viscoplastic constitutive models suitable for creep". In: *International journal for numerical methods in engineering* 53.3, pp. 637–652.

Sierra/SolidMechanics Mar. 2021. *Sierra/SolidMechanics User's Guide.* 5.0. SAND2021-2961. Sandia National Laboratories. Albuquerque, NM, USA; Livermore, CA, USA.

Sobolik, S. R. Mar. 2022. *Typical gas storage cavern loading cycles.* Personal Communication.

Spiers, C., Schutjens, P., Brzesowsky, R., Peach, C., Liezenberg, J., and Zwart, H. 1990. "Experimental determination of constitutive parameters governing creep of rocksalt by pressure solution". In: *Geological society, London, special publications* 54.1, pp. 215–227.

Yahya, O., Aubertin, M., and Julien, M. 2000. "A unified representation of the plasticity, creep and relaxation behavior of rocksalt". In: *International journal of rock mechanics and mining sciences* 37.5, pp. 787–800.